LAWRENCE
LIVERMORE
NATIONAL
LABORATORY

LLNL-JRNL-699377

# Zonal Flow Generation in Inertial Confinement Fusion Implosions

J. L. Peterson, K. D. Humbird, J. E. Field, S. T. Brandon, S. H. Langer, R. C. Nora, B. K. Spears

August 2, 2016

Physics of Plasmas

## Disclaimer

# Zonal Flow Generation in Inertial Confinement Fusion Implosions

J. L. Peterson,[1, a)] K. D. Humbird,[1, 2] J. E. Field,[1] S. T. Brandon,[1] S. H. Langer,[1] R. C. Nora,[1] B. K. Spears,[1] and P. T. Springer[1]

[1)] *Lawrence Livermore National Laboratory, Livermore, California, USA*

[2)] *Texas A&M University, College Station, Texas, USA*

(Dated: 3 February 2017)

A supervised machine learning algorithm trained on a multi-petabyte dataset of inertial confinement fusion simulations has identified a class of implosions that robustly achieve high yield, even in the presence of drive variations and hydrodynamic perturbations. These implosions are purposefully driven with a time-varying asymmetry, such that coherent flow generation during hotspot stagnation forces the capsule to self-organize into an ovoid, a shape that appears to be more resilient to shell perturbations than spherical designs. This new class of implosions, whose configurations are reminiscent of zonal flows in magnetic fusion devices, may offer a path to robust inertial fusion.

## I. INTRODUCTION

The aim of inertial confinement fusion (ICF)[1] is to compress a hollow shell of cryogenic deuterium-tritium (DT) fuel to thermonuclear conditions. In the case of direct or indirect drive, the spherical ice shell is encased in an ablator material, the outer surface of which is heated either directly by impinging laser beams or indirectly via x-rays in an encasing *hohlraum*, respectively. As the capsule surface ablates, the spherical shell compresses to high temperature and density. The goal is to have the gas at the center of the shell ignite a fusion burn wave, which consumes the DT shell and releases large amounts of fusion energy.

However, this process can be sensitive to hydrodynamic instabilities, which can arise throughout the implosion. At early times, shocks can cause the Richtmyer-Meshkov[2–4] growth of small-scale imperfections, which can be amplified by the Rayleigh-Taylor (RT) instability[5–7] during the main capsule acceleration. As the capsule compresses, the back-pressure exerted by the central gas on the shell causes the shell to decelerate, at which point the inner surface of the shell becomes RT unstable. During this time, a perturbation of wave number $k$ on the inner surface of a shell with characteristic density scale length $L_m$ and local ablation velocity $v_a$ (due to mass ablating into the forming hot spot) that experiences a deceleration of magnitude $g$ will grow with a growth rate of the form[8]:

$$\gamma_{RT} = \alpha\sqrt{\frac{kg}{1+kL_m}} - \beta k v_a, \tag{1}$$

for some constants $\alpha \simeq 0.9$ and $\beta \simeq 1.4$. Under converging geometry, Bell-Plesset-like (BP) effects[9,10] can enhance this growth, such that the total linear growth from any perturbation increases with the convergence ratio $R(t=0)/R(t)$ of the shell.

In sum, these processes can lead to a distorted asymmetric shell at stagnation, which adversely affects performance. For example, the ITF formalism[11] defines an ignition metric that depends on (among other things) the hotspot radius $R_{hs}$ and the mode-weighted RMS deviation from that hotspot $\Delta R_{hs}$:

$$\text{ITF} \propto \left(1 - 1.2\frac{\Delta R_{hs}}{R_{hs}}\right)^4. \tag{2}$$

Larger values of ITF are more robust ignitors, and ITF can be used to estimate a capsule's margin. For instance, a hotspot deviation $\Delta R_{hs}/R_{hs}$ of 0.13 can reduce the margin for ignition by a factor of two. Other studies[12–14] have also found that capsule performance degrades when implosions are asymmetric.

Because non-radial capsule stagnation is so detrimental to performance, one of the major goals of ICF research is to produce a nearly spherical implosion. One way to accomplish this is via the minimization of the seeds for asymmetric stagnation. Examples include placing engineering tolerances on the capsule surfaces[15], reducing the effective footprints of the capsule support tent[16] and DT gas fill tube[17], and ensuring a smooth capsule drive[13,18]. Additionally, one can attempt to reduce the total integrated linear growth of hydrodynamic instabilities, by exploring such techniques as adiabat shaping[19–28] or by pursuing implosions with low convergence ratios[29].

In this work, we report on a *nonlinear* stabilization process for ICF implosions that simultaneously addresses drive and shell distortions. In particular, intentionally generated large scale coherent flows within the hotspot can stabilize other shell deformations that arise during stagnation. These flows, which are reminiscent of the zonal flows that appear in planetary atmospheres[30] and magnetic fusion devices[31], shear off both smaller scale instabilities and larger scale asymmetries, making these implosions more robust than those without zonal flows.

Implosions with these flows are not spherical, but rather asymmetric, with the shell forming an ovoid during capsule deceleration and stagnation. Their high performance challenges the notion expressed in Eq. 2 that spherical shells universally have the largest ignition mar-

[a)] peterson76@llnl.gov

gins.

This robust aspherical implosion was discovered by a machine learning algorithm trained on the largest ICF capsule simulation dataset ever created. We discuss the dataset, the learning algorithm and how it predicted the existence of the ovoid in Sec. II. In Sec. III, we confirm the algorithm's prediction with a series of new simulations at the predicted robust point and show that these implosions are more resilient to distortions driven by asymmetric drives and the capsule support tent than those driven symmetrically. Section IV summarizes and discusses our results.

## II. FINDING A ROBUST IMPLOSION

Our study builds on previous efforts[12–14,32] to use large ensembles of simulations to quantify the performance of implosions under adverse conditions. Here, we are interested in taking the further step of using data science techniques to search for implosions that exist in flat regions of parameter space, thus being explicitly robust to perturbations around their design point. That is, we want to not just quantify robustness, but optimize for it.

The methodology is straightforward: choose a baseline implosion design, generate a suite of multi-dimensional simulations of perturbations around that baseline and fit the resultant quantity of interest $\mathcal{Q}$ (for instance, the total produced yield) to a functional form of the $i$ individual input variations $\bar{x} \in \mathbb{R}_d = \{x_i\}$, thereby creating a data-trained surrogate model $\tilde{\mathcal{Q}} \simeq \mathcal{Q}$ that can be quickly evaluated for any value of $\bar{x}$, not necessarily included in the original simulation ensemble. One can then use $\tilde{\mathcal{Q}}$ to optimize $\bar{x}$ for robustness without performing additional simulations.

In studies[12–14,32] that produce rules like Eq. 2, the surrogate model is assumed to be a power-law of the form:

$$\tilde{\mathcal{Q}}(\bar{x}) = \prod_i^d f_i \left(x_i\right)^{a_i}, \tag{3}$$

with $f_i(x_i)$ some analytic function of the input parameters, such as $(1 - b_i x_i)$, for some constant $b_i$. It is also possible as in Eq. 2 for the $x_i$ not to be simulation input parameters, but rather physical quantities extracted from the simulation database, like $\Delta R/R$.

Laws like Eq. 3 are easy to construct (being linear regression on $\log f_i$) and interpret (since the relative strengths and impacts of the various terms come directly from the constants $a_i$ and $b_i$). They can built with datasets of a few hundred[14] or a few thousand[12,13,32] individual simulations. However, Eq. 3 precludes any interactions between the $x_i$, and the $a_i$ are held constant over the entire space. This makes power laws unsuitable for design optimization, particularly when the $x_i$ are simulation input parameters.

Instead, to search for a robust implosion, we look to the family of non-parametric $\tilde{\mathcal{Q}}$, such as those generated by machine learning statistical algorithms. These methods do not necessarily make assumptions about the underlying structure or functional form of $\mathcal{Q}$, but can require many simulations to achieve an acceptable level of accuracy, especially when the input space is of high dimensionality ($d > 4$). However, recent work[33] has shown that machine learning techniques can build accurate surrogate models from ICF simulation ensembles (without alpha-particle deposition) of $d = 7$ with $\sim 3500$ simulations.

In this section, we build off this successful application of machine learning to construct surrogate models for ICF implosions and search for a design that ignites even under adverse conditions. We explain our new dataset that consists of a nine-dimensional survey of drive amplitudes, asymmetries and convergence ratios, and use machine learning techniques to build surrogate models for multiple quantities of interest. We then combine these surrogates, which effectively serve as fast but complex interpolators for our dataset, into a robustness cost function that is suitable for optimization and find a set of input parameters that produce the optimally robust implosion. Next, we query additional surrogates, which are trained on the individual Legendre moments of the DT fuel shape, and find that the optimal input parameters produce an ovoid shape at stagnation. The surrogate models also predict that the optimal ovoid-shaped implosion is more resilient to a variety of perturbations than the baseline spherical implosion. In Section III, additional simulations at the optimal point (which are not in the original dataset) confirm the surrogate predictions and provide physical insight into the high performance of this implosion.

### A. The Trinity Open Science I Dataset

The first step towards searching for a robust design is to create a large dataset of input simulations, upon which to build a surrogate model. Our new ensemble of approximately 60,000 two-dimensional ICF capsule simulations is the largest created to date.

Consuming roughly 39 million cpu-hours of computer resources during the Open Science Phase I of the Trinity Supercomputer at Los Alamos National Laboratory, the dataset constituted a nine-dimensional parameter scan of time-varying drive magnitudes, drive asymmetries (described by Legendre modes 1, 2 and 4, $P_n$), and capsule gas fill densities. Due to its large size, the estimated 5 petabytes of raw data were processed using a novel *in-transit* data analysis technique[34], which used internal servers (built on the beanstalkd library[35]) to direct dedicated compute nodes to analyze and erase raw data on-the-fly before overflowing the file system.

The baseline simulation, run with the radiation hydrodynamics code HYDRA[36], is an axisymmetric variant of a high-density-carbon (HDC)[37] National Ignition Facility (NIF)[38] implosion design, meant to ignite in 1D, with a 20 $\mu$m dopant layer of 3% Si embedded in the

75 $\mu$m-thick shell of 1108 $\mu$m outer radius. Both the DT and the HDC use tabular equations of state (LEOS 1018 and 64 respectively[39,40]) and opacities. The ice layer is 55 $\mu$m thick and the central gas has a baseline density of $5 \times 10^{-4}$ g/cm$^3$. The initially Arbitrary-Lagrangian-Eulerian mesh with 513 angular zones and 321 impedance matched radial zones remaps to an entirely Eulerian elliptic mesh near stagnation to trade accuracy for robustness (99.9% of the simulations completed without human intervention). The nine-dimensional study constitutes latin hypercube sampling of a space around the baseline implosion, with linearly varying drive magnitude $A$ and asymmetry perturbations between three time points (the end of the first shock "trough," the end of the "rise" to peak laser power and the end of "peak" radiation drive). All time-dependent perturbations ramp up from time zero and down from the end of peak power. $P_1$ and $P_4$ have the same value at the three time points, but $P_2$ and $A$ can vary (see Fig. 1a for an example). The peg points are sampled linearly between $\pm$ [2, 10, 5, 25]% for [$P_1$, $P_2$, $P_4$, $A$]. The capsule gas fill density is sampled logarithmically between 0.2× and 5×, for a total of 9 independent variables.

### B. Using Machine Learning to Search for a New Design

With the dataset in hand, it is possible to use machine learning techniques to build surrogate models that infer the behavior of multiple quantities of interest at any point within our design space, even where no simulations exist. Here, we opt to use random forest regression[41], which consists of a series of bootstrapped decision trees trained on subsets of the whole dataset. As such, a random forest can handle large quantities of high-dimensional data and automatically incorporate nonlinearities, which becomes especially important near regions of high yield that are potentially surrounded by steep "cliffs."

We find that such a random forest regression surrogate for the logarithm of the total energy yield ($\log_{10} Y$) achieves an 80% cross-validation mean error of 8%. (Explicitly we train the surrogate model on a random 80% of the data and test the prediction against the other 20%: the mean error on the prediction for the 20% random hold-out points is 8%.) Being a statistical fit to our entire data set, the yield surrogate not only allows for the continuous real-time interpolation of parameter space between our discrete samples, but also lets us define a metric for robustness. For this measure, we pick a point in parameter space and with the surrogate make 1000 random input variations within a hypercube centered at that location with side length $\Delta$ of 10% of the total sample space. The number of surrogate evaluations that achieve $Y > 1$ MJ serves as a local estimate of the probability of achieving high yield under variable conditions: $\mathcal{P}(Y > 1|\Delta = 0.1)$. This function serves as a smoothing operator on the yield, filtering out narrow "peaks" of high performance in favor of more broad "plateaus."

We can also build surrogates for any number of the extracted physical quantities, such as DT fuel areal density ($\rho R$), the first Legendre moments of the DT shell ($P_{0-8}$) and an ignition threshold factor metric[42] $ITFX \doteq Y(\rho R)^2$ ("ignition" $\doteq ITFX \gtrsim 1$) at the time of peak energy production ("bang time").

Finally by combining the surrogate models, we can define a cost function for multi-dimensional optimization that similarly weights robustness and yield:

$$\mathcal{C} = 10\mathcal{P} + ITFX. \tag{4}$$

The first term in Eq. 4 finds broad areas of parameter space that ignite, and the second term finds locations that are high up the ignition cliff. To speed up convergence toward an optimal point, we weight the first term higher (which being a probability maximizes at 1) to make it of similar order as the second term (which crosses the ignition threshold at 1, but can be 10 or higher for robustly burning designs). Furthermore, since our operational space is nine-dimensional and a single evaluation of $\mathcal{P}$ requires 1000 surrogate evaluations, we opt for a simplex based optimization algorithm[43] to avoid gradient evaluations in our search for a robust design.

Optimization of Eq. 4 produces the drive shown in Fig. 1a (additionally, the optimal point has a 0.5× gas fill multiplier). Notably, this optimal point, which is predicted to robustly achieve high yield, has a time-varying $P_2$ drive asymmetry. Figure 1b compares the DT bang-time fuel shapes as predicted by the $P_n$ surrogate models for both the baseline and optimal drives. Due to the time-varying asymmetry, the optimal drive's stagnated shape is predicted not to be a sphere, but rather an ovoid.

The surrogates also predict that the optimal ovoid-producing drive is more resistant than the symmetrically driven baseline to other perturbations. Figure 2 shows surrogate outputs for yield under changing peak drive multiplier, represented by the total drive fluence $\int T_r^4 dt$ (normalized to the baseline). This metric serves as an estimate of the total laser energy required to achieve a given radiation drive. To eliminate the effects of the remaining drive parameters, the optimal and symmetric implosions are compared with the same gas fill, $P_1$, and $P_4$ perturbations such that the change in performance is due to the $P_2$ drive alone. Both designs fall off in yield as the drive is reduced. However, while adding a +2% $P_1$ to the baseline design makes ignition impossible for any drive in our parameter space, the location of the optimal point's ignition cliff remains unchanged at 1.05 total fluence.

To investigate further the movement of the ignition cliff, yield contours predicted by the surrogate are shown in Fig. 3a for varying $P_2$ drives on the rise to peak power ($P_2^R$) and at the end of the peak radiation drive ($P_2^P$). The overlaying white contour lines correspond to the surrogate-predicted $P_2$ moment of the fuel at bang time, and the orange point indicates the location of the optimal

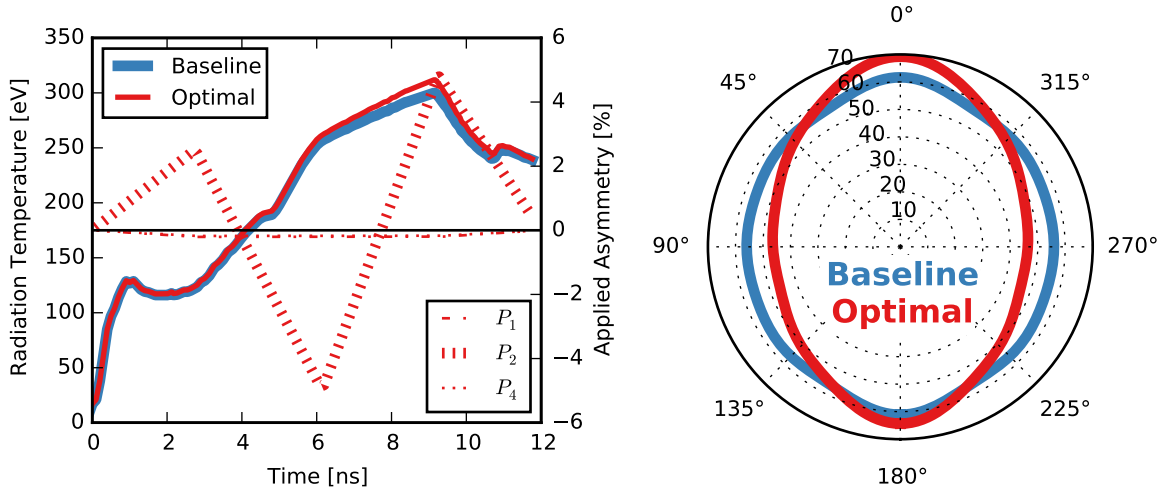


(a) Capsule radiation drives

(b) Bang time fuel shapes ($\mu$m)

FIG. 1. Comparison of the baseline and optimal radiation drives and surrogate-predicted bang time fuel shapes.

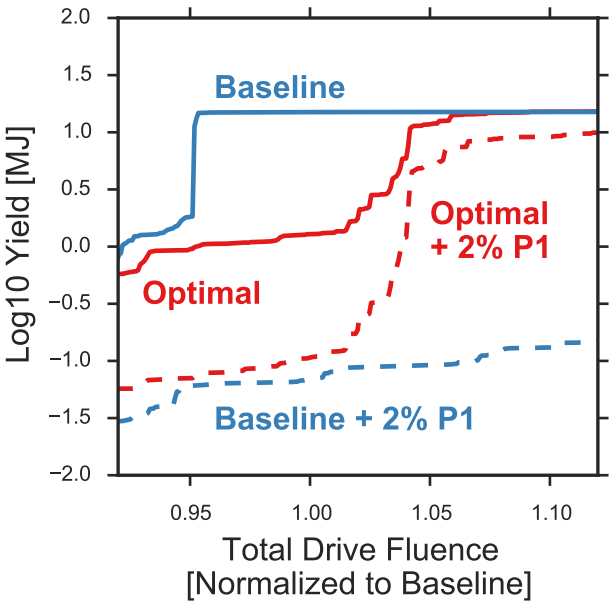


FIG. 2. The surrogate's estimate of yield under changing peak drive, as represented by the total normalized drive fluence $\int T_r^4 dt / (\int T_r^4 dt)_{baseline}$ for the baseline (round) and optimal (ovoid) cases. Unlike the baseline, the optimal point can ignite for fluences $> 1.05$, even with an applied $P_1$.

implosion. There is a broad, high-yield ridge along a line of compensating $P_2^R$ and $P_2^P$ drives, with higher yields favoring a negative $P_2^R$ and positive $P_2^P$. This compensating drive does not result in a round implosion, but rather an ovoid with positive $P_2$ ($\simeq 20\%$) (see Fig. 3b for the reconstructed fuel shapes at the colored points). Under the addition of a $P_1$ perturbation, the high-yield ridge contracts toward more extreme compensating drives. The optimal implosion remains within the ridge boundaries, while the round implosion falls to low yield. Additionally, the high-yield ridge appears to extend beyond the boundaries of the design space, suggesting that there may exist an implosion with higher performance than the optimal point if more extreme compensating $P_2$ drive perturbations are considered, outside the bounds of our dataset. In summary, the surrogate predictions in Figs. 3a and 3b show that the optimal point sits on a topological ridge in parameter space defined by compensating $P_2$ drives of opposite signs. More extreme variations in drive $P_2$ are more robust to other perturbations. The high-yield ridge corresponds not to round implosions, but rather ovoids with bang-time fuel shapes given by $P_2/P_0 \simeq 20\%$.

## III. NEW HYDRA SIMULATIONS OF THE ROBUST DESIGN

To confirm the surrogates' predictions of a robust ovoid at a location not explicitly in the original simulation database, a series of 2D HYDRA simulations were performed for the optimal point and for a symmetric simulation with the same drive amplitude and gas fill, so that any differences are due solely to the time-varying drive asymmetry. To isolate alpha-particle bootstrapping from hydrodynamic effects, "burn-off" simulations with a reduced fusion cross-section were also performed (with their total reported yields re-scaled by the same factor for comparison to the full "burn-on" cases.) For these conditions, the surrogate predicts 17.4 MJ for the burn-on symmetric implosion and 15.2 MJ for the ovoid. Firstly HYDRA confirms the predicted high performance for the optimal point ($Y_{burn-on} = 16.6$ MJ,

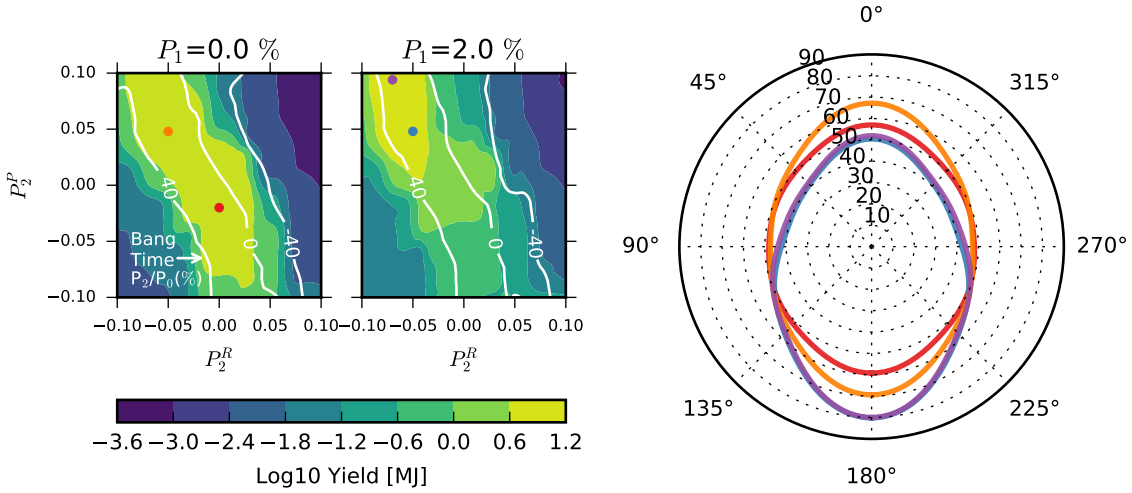


(a) Yields and bang time fuel $P2/P0$.

(b) Select bang time fuel shapes ($\mu$m).

FIG. 3. (a) Contours of the surrogate predictions for the yield and bang time fuel $P_2/P_0$ for varying applied drive $P_2$ on the rise to peak power ($P_2^R$) and at the end of the peak radiation drive ($P_2^P$), with and without an applied $P_1$ perturbation. The reconstructed fuel shapes from the $P_0 - P_8$ surrogates at the colored dots are plotted in (b). The orange point indicates the optimal implosion. High-yield implosions lie along a ridge of compensating $P_2$ drives (negative on the rise, positive at the peak), with the ridge shifting to require more extreme drives to reduce the effects of $P_1$. The $P_2$ drives that correspond to the high-yield ridge produce ovoid implosions with positive $P_2/P_0 \simeq 20\%$.

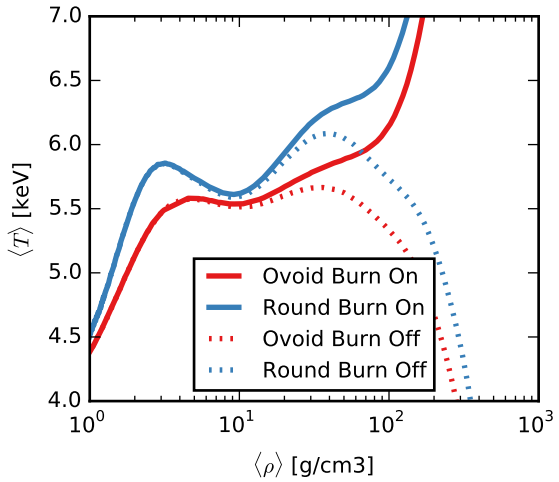


FIG. 4. Trajectories in DT burn-rate weighted density and temperature for the ovoid and round implosions (with and without alpha-particle heating). The ovoid compresses and burns at lower temperatures and higher densities than the round implosion.

$Y_{burn-on}/Y_{burn-off} = 355$ for the ovoid vs. 17.2 MJ and 262 for round). This corresponds to a burn-on yield-over-1D of 97%, but a burn-off yield-over-1D of only 71%.

To understand this phenomenon, we turn to Fig. 4, the trajectories of DT burn-rate averaged temperature and density for the round and ovoid implosions. The ovoid implosion compresses and burns at a higher density and lower temperature than the round case. Since the ICF hotspot self-heating condition can be written as $f(\rho R) > g(T)$ for some functions $f$ and $g$[1], the higher density and lower temperature ovoid burn trajectories in Fig. 4 imply a more efficient burn process. This helps to explain the near 1-D full burn yield.

Additionally, HYDRA shows how an ovoid shape arises explicitly from the time-dependent implosion dynamics. Asymmetric shock bounce (that begins deceleration) seeds vorticity in the gas. The negative $P_2$ drive on the rise to peak power biases the capsule compression equatorially. As the compressed gas meets on axis, it forms axial jets. The late time positive $P_2$ drive prevents the jets from escaping and the flow circles on itself, forming two co-axial counter-propagating vortex rings, and the hotspot organizes during stagnation into a configuration shown in Fig. 5. As shown, the exterior shell conforms to the vortex rings (forming an ovoid) and the central gas between the vortexes becomes trapped in a vorticity quadrupole. The hotspot is elongated, and does not align with the high-pressure central core. Strong coherent flows exist throughout the hotspot, so that the cold dense shell on the equator accretes into the central high-pressure region, burns, and exhausts via the poles. Interestingly enough, one can estimate a single fluid element taking $\sim 0.5$ ns to make a complete revolution of the eddies shown in Fig. 5, longer than typical ($\lesssim 0.1$ ns) ICF burn and disassembly times.

These flows appear to nonlinearly suppress the growth of hydrodynamic instabilities. Figure 6 shows the upper right section of the stagnating shell for a burn-off ovoid

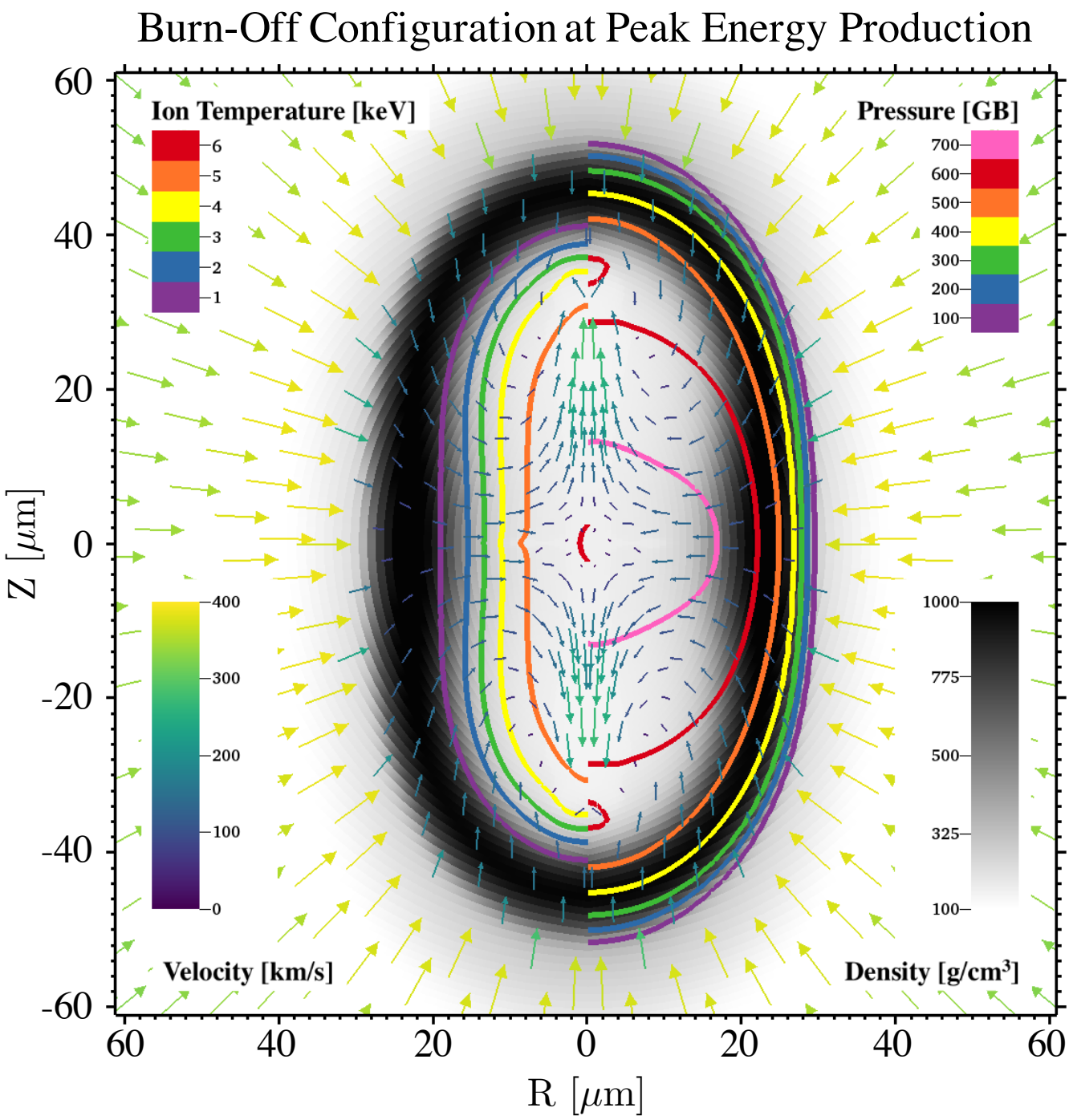


FIG. 5. Velocity (arrows), density (gray), ion temperature (left color contours), and pressure (right color contours) at the time of peak energy production for a burn-off HYDRA simulation of the ovoid implosion.

implosion with added roughness on the inner ice surface (at NIF ignition specifications[11]) and a perturbation on the ablator surface due to the capsule support tent (calibrated to a 100 nm tent on an HDC capsule[44]). Two key distortions are worth noting. Firstly, a large on-axis jet, originally seeded by ice surface roughness, is entrained in a large axial flow field, directed down toward the central hotspot. Secondly, the shell has a visible low-density "scar" due to the tent. However, the background flow meets the axis jet head-on, forms a high velocity ($> 300$ km/s) shearing layer and directs the jet away from the hotspot. The same shear layer directs the flow field tangential to the tent scar, reducing convective loss through the tent hole.

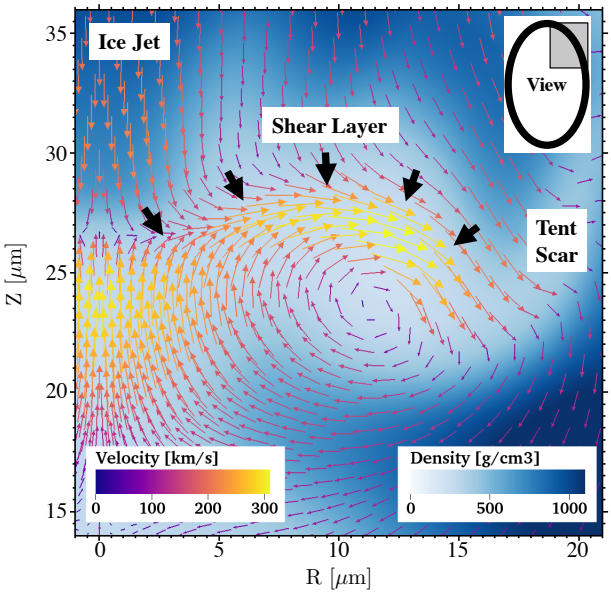


FIG. 6. Density and velocity fields in the upper part of the stagnating shell for an ovoid burn-off HYDRA simulation perturbed with ice layer roughness and capsule support tent membrane. The background flows set up a high-velocity shear layer (thick arrows) that mitigates the effects of the perturbations during stagnation.

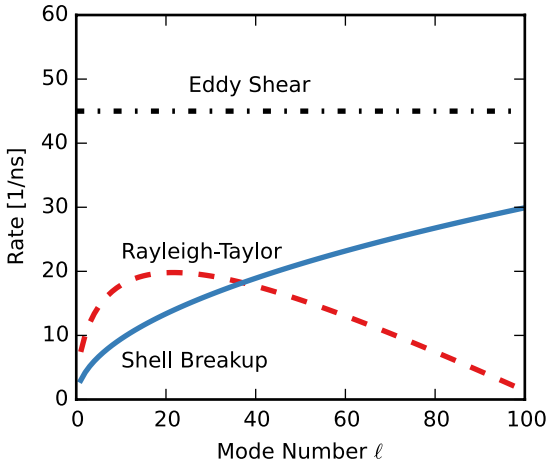


FIG. 7. The local shearing rate of the eddy in Fig. 6 is larger than both the deceleration Rayleigh-Taylor growth rate (Eq. 1) or the shell breakup rate (Eq. 5).

The shearing in Fig. 6 appears strong enough to compete with shell distortions that occur during deceleration. The local shear rate can be estimated as the ratio of the local velocity to the eddy size. The eddy in Fig. 6 is roughly 5 $\mu$m across with an average velocity of $(150 + 300)/2 = 225$ $\mu$m/ns, which gives a shearing rate of 45 ns$^{-1}$. Meanwhile, perturbations on the shell evolve at a characteristic rate that can be estimated as either the RT growth rate (given by Eq. 1) or the inverse of the

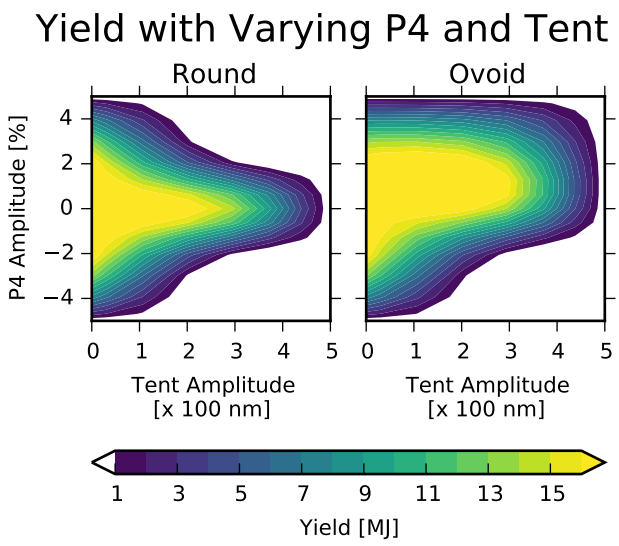


FIG. 8. Contours of yield for the round and ovoid implosions under combination $P_4$ drive asymmetry and tent perturbation amplitude.

shell breakup time $\tau$[45]:

$$\tau = \sqrt{\frac{2\pi R\,(\rho R)_{shell}}{l P_{stag}}}, \tag{5}$$

for some mode number $l = kR$ on a shell with areal density $(\rho R)_{shell}$ stagnating against a hotspot with pressure $P_{stag}$. Figure 7 shows that the eddy shear rate is larger than both rates predicted by Eqs. 1 and 5, suggesting that the shear flows present in the ovoid are potentially strong enough to impact the growth of shell perturbations during capsule deceleration.

Overall, these ovoid implosions can tolerate larger distortions than their round counterparts. Figure 8 shows contours of yield $> 1$ MJ for the round and ovoid implosions with varying levels of applied $P_4$ asymmetry and tent amplitude. The performance of both implosions falls off with increasing perturbation strength, but the ovoid implosion maintains high yield for a larger parameter range. For instance, the ovoid produces $> 9$ MJ with a 300 nm tent and +3% $P_4$, where the round implosion fails to ignite.

In all, these new simulations confirm the surrogates' predictions of an asymmetric ovoid implosion that is more resilient to perturbations than symmetrically driven one-dimensional designs.

## IV. DISCUSSION AND CONCLUSIONS

In summation, we report the discovery of a new class of ICF implosions, which were found with machine learning techniques as applied to the largest ensemble of ICF simulations to date. Firstly, these implosions are ovoid in

shape, challenging the philosophy behind formalisms like Eq. 2 that suggest spherical implosions uniformly outperform aspherical ones. Secondly, they are intentionally driven by strong time-varying drive asymmetries, which serve to set up large-scale coherent convective flows at stagnation. Thirdly, they are more robust than spherical implosions to shell perturbations from either drive asymmetries or the hydrodynamic growth of smaller-scale shell imperfections, perhaps due to locally strong shearing rates induced by said flows.

Although the ovoids challenge the notion that the ideal implosion is symmetric (that asymmetries always degrade performance), they are not inconsistent with some studies[46] and anecdotal observations[47,48] of improved performance with positive $P_2$ shapes.

Interestingly enough, our results may be related to other naturally occurring phenomena. The key features of the ovoid are the large-scale convective flows that circulate into the hotspot on the equator and out via the poles. In fluid dynamics, the upper and lower solutions are repelling circular vortexes[49] (like smoke rings and mushroom clouds) joined by a Burger's vortex at the origin[50], all of which are axially symmetric 3D fluid solutions with increased stability at low Reynolds numbers[51,52], like those expected in ICF hotspots[53].

This flow pattern is similar to that proposed to exist in the Jovian core that drives the large zonal flows on the planet's surface[30]. Zonal flows also play a prominent role in the stabilization of magnetic fusion drift wave turbulence[31]. These waves, like the Rossby waves in planetary atmospheres experience an inverse cascade phenomenon, in which small scale perturbations can nonlinearly couple energy into larger scales. As such, larger scale flows can serve as energy sinks for smaller scales by shearing away perturbations as they grow.

The ovoid implosions could be experiencing a similar process. In this scenario, since nonlinear Rayleigh-Taylor bubble merger[54] can be thought of as an inverse cascade process (smaller bubbles merge into large bubbles), the stabilization of small-scale perturbations by larger scale flows could occur during the capsule stagnation phase. From this view, the flow fields induced in the ovoid implosion protect the hotspot from shell imperfections during stagnation by serving as an energy sink for smaller scale shell instabilities, shearing away unstable shell imperfections. In other words, the central hotspot is not in a hydrostatic equilibrium, but rather a nonlinear hydro*dynamic* one, dominated by coherent convective flow.

That zonal flows could be induced in ICF implosions is an interesting prospect, because they would allow for a nonlinear mechanism for the stabilization of stagnating shells. However, this stabilization would not come without a price, as Fig. 2 shows that the required energy to ignite an oval implosion is indeed higher than a perfectly spherical implosion (roughly 8%). In this sense, the ovals intentionally contain a finite amount of residual hotspot kinetic energy at stagnation, but that energy is coherently organized in a stabilizing flow pattern, trading one-dimensional margin for robustness in higher dimensions.

Such a new class of implosions opens many avenues of future work. First, the exact and optimal generation conditions of ICF zonal flows must be explored. An analytic model of stagnation that includes these nonlinear flows could be extremely helpful in that regard. Additional analytic work would involve mapping out and exploring the turbulent energy channels that govern the interactions of the zonal flows and smaller scale shell perturbations.

Additional increasingly complex simulations are also warranted. Although our simulations impose an axisymmetric constraint and are limited to two-dimensional configurations, both the Burger's vortex and the spherical vortex are stable axisymmetric configurations that exist in natural (3D) systems (for instance, smoke rings). Variations on these flows also exist in 3D, often with rotation about the z-axis (as in hurricanes and tornados). Exploring the stability and generation of these configurations in 3D is therefore a top priority. Furthermore, these flow patterns are likely to induce magnetic fields, which may alter the stability properties of the implosion (or perhaps offer a means of experimentally diagnosing their existence[55]). It is also yet to be seen if these implosions are more or less sensitive to variations and uncertainties in other physics models, such as thermal conductivity, equations of state, viscosity, implosion adiabat, or velocity. Again, this is another area where an analytic stagnation flow model may prove useful.

Finally, it may be possible to experimentally create these implosions on current facilities. Near-vacuum hohlraums (NVH)[56], which are designed to counter a late-time polar drive with early time equatorial drive, may already operate near this regime (indeed similar flow patterns have been observed in some integrated NVH simulations of current NIF designs[57]). The predicted existence of a high-yield ridge in parameter space could be tested with a controlled experimental campaign that uses the ratio of the powers on NIF's inner and outer cones to independently vary the x-ray $P_2$ during the rise and peak of the laser pulse. Furthermore, given their inherent asymmetry, these configurations may be approachable in a NIF polar direct drive configuration[58]. Mapping out the experimental signatures of zonal flow dominated hotspots is therefore another priority.

In conclusion, we report the discovery of a class of high-performing asymmetric implosions that are more robust to drive and shell perturbations than those driven symmetrically. Suggested by a machine learning algorithm trained on a large simulation dataset, their existence not only opens the possibility of a new type of counterintuitively stable implosion, but also demonstrates the potential benefits of augmenting physics studies with data science.

## ACKNOWLEDGMENTS

The authors wish to thank S. Hatchett, H. Robey, J. Hammer, M. Buchoff, J. Gaffney, D. Munro, O. Hurricane, P. Patel, P. Robinson, L. F. Berzak Hopkins, M. Rosen, D. Callahan, N. Meezan, K. Anderson, J. Knauer and R. Betti for fruitful discussions. K. H. was supported by the LLNL High Energy Density Physics Summer Student Program. The simulation ensemble database was completed on the Trinity supercomputer at Los Alamos National Laboratory thanks to the Phase I Open Science Campaign. This work was performed under the auspices of the U.S. Department of Energy by Lawrence Livermore National Laboratory under Contract DE-AC52-07NA27344. Document released as LLNL-JRNL-699377.

[1] S. Atzeni and J. Meyer-ter-Vehn, *The Physics of Inertial Fusion* (Oxford Science Publications, 2004).
[2] E. E. Meshkov, Fluid Dynamics **4**, 101 (1969).
[3] R. D. Richtmyer, Communications on Pure and Applied Mathematics **13**, 297 (1960).
[4] J. L. Peterson, D. S. Clark, L. P. Masse, and L. J. Suter, Physics of Plasmas **21**, 092710 (2014).
[5] Rayleigh, Proceedings of the London Mathematical Society **s1-14**, 170 (1882).
[6] G. Taylor, Proceedings of the Royal Society of London. Series A. Mathematical and Physical Sciences **201**, 192 (1950).
[7] R. Betti, V. N. Goncharov, R. L. McCrory, and C. P. Verdon, Physics of Plasmas **5**, 1446 (1998).
[8] J. Sanz and R. Betti, Physics of Plasmas **12**, 042704 (2005).
[9] M. S. Plesset, Journal of Applied Physics **25**, 96 (1954).
[10] V. N. Goncharov, P. McKenty, S. Skupsky, R. Betti, R. L. McCrory, and C. Cherfils-Clérouin, Physics of Plasmas **7**, 5118 (2000).
[11] S. W. Haan, J. D. Lindl, D. A. Callahan, D. S. Clark, J. D. Salmonson, B. A. Hammel, L. J. Atherton, R. C. Cook, M. J. Edwards, S. Glenzer, A. V. Hamza, S. P. Hatchett, M. C. Herrmann, D. E. Hinkel, D. D. Ho, H. Huang, O. S. Jones, J. Kline, G. Kyrala, O. L. Landen, B. J. MacGowan, M. M. Marinak, D. D. Meyerhofer, J. L. Milovich, K. A. Moreno, E. I. Moses, D. H. Munro, A. Nikroo, R. E. Olson, K. Peterson, S. M. Pollaine, J. E. Ralph, H. F. Robey, B. K. Spears, P. T. Springer, L. J. Suter, C. A. Thomas, R. P. Town, R. Vesey, S. V. Weber, H. L. Wilkens, and D. C. Wilson, Physics of Plasmas **18**, 051001 (2011).
[12] D. S. Clark, S. W. Haan, and J. D. Salmonson, Physics of Plasmas **15**, 056305 (2008).
[13] A. L. Kritcher, R. Town, D. Bradley, D. Clark, B. Spears, O. Jones, S. Haan, P. T. Springer, J. Lindl, R. H. H. Scott, D. Callahan, M. J. Edwards, and O. L. Landen, Physics of Plasmas **21**, 042708 (2014).
[14] J. Gu, Z. Dai, Z. Fan, S. Zou, W. Ye, W. Pei, and S. Zhu, Physics of Plasmas **21**, 012704 (2014).
[15] S. W. Haan, H. Huang, M. A. Johnson, M. Stadermann, S. Baxamusa, S. Bhandarkar, D. S. Clark, V. Smalyuk, and H. F. Robey, Physics of Plasmas **22**, 032708 (2015).
[16] S. R. Nagel, S. W. Haan, J. R. Rygg, M. Barrios, L. R. Benedetti, D. K. Bradley, J. E. Field, B. A. Hammel, N. Izumi, O. S. Jones, S. F. Khan, T. Ma, A. E. Pak, R. Tommasini, and R. P. J. Town, Physics of Plasmas **22**, 022704 (2015).
[17] T. R. Dittrich, O. A. Hurricane, L. F. Berzak-Hopkins, D. A. Callahan, D. T. Casey, D. Clark, E. L. Dewald, T. Doeppner, S. W. Haan, B. A. Hammel, J. A. Harte, D. E. Hinkel, B. J. Kozioziemski, A. L. Kritcher, T. Ma, A. Nikroo, A. E. Pak, T. G. Parham, H.-S. Park, P. K. Patel, B. A. Remington, J. D. Salmonson, P. T. Springer, C. R. Weber, G. B. Zimmerman, and J. L. Kline, Journal of Physics: Conference Series **717**, 012013 (2016).
[18] R. P. J. Town, D. K. Bradley, A. Kritcher, O. S. Jones, J. R. Rygg, R. Tommasini, M. Barrios, L. R. Benedetti, L. F. B. Hopkins, P. M. Celliers, T. Döppner, E. L. Dewald, D. C. Eder, J. E. Field, S. M. Glenn, N. Izumi, S. W. Haan, S. F. Khan, J. L. Kline, G. A. Kyrala, T. Ma, J. L. Milovich, J. D. Moody, S. R. Nagel, A. Pak, J. L. Peterson, H. F. Robey, J. S. Ross, R. H. H. Scott, B. K. Spears, M. J. Edwards, J. D. Kilkenny, and O. L. Landen, Physics of Plasmas **21**, 056313 (2014).
[19] K. Anderson and R. Betti, Physics of Plasmas **11**, 5 (2004).
[20] R. Betti, K. Anderson, J. Knauer, T. J. B. Collins, R. L. McCrory, P. W. McKenty, and S. Skupsky, Physics of Plasmas **12**, 042703 (2005).
[21] S. E. Bodner, D. G. Colombant, J. H. Gardner, R. H. Lehmberg, S. P. Obenschain, L. Phillips, A. J. Schmitt, J. D. Sethian, R. L. McCrory, W. Seka, C. P. Verdon, J. P. Knauer, B. B. Afeyan, and H. T. Powell, Physics of Plasmas **5**, 1901 (1998).
[22] J. H. Gardner, S. E. Bodner, and J. P. Dahlburg, Physics of Fluids B **3**, 1070 (1991).
[23] V. N. Goncharov, J. P. Knauer, P. W. McKenty, P. B. Radha, T. C. Sangster, S. Skupsky, R. Betti, R. L. McCrory, and D. D. Meyerhofer, Physics of Plasmas **10**, 1906 (2003).
[24] J. P. Knauer, K. Anderson, R. Betti, T. J. B. Collins, V. N. Goncharov, P. W. McKenty, D. D. Meyerhofer, P. B. Radha, S. P. Regan, T. C. Sangster, V. A. Smalyuk, J. A. Frenje, C. K. Li, R. D. Petrasso, and F. H. Séguin, Physics of Plasmas **12**, 056306 (2005).
[25] J. L. Peterson, L. F. Berzak Hopkins, O. S. Jones, and D. S. Clark, Phys. Rev. E **91**, 031101 (2015).
[26] H. F. Robey, V. A. Smalyuk, J. L. Milovich, T. Döppner, D. T. Casey, K. L. Baker, J. L. Peterson, B. Bachmann, L. F. Berzak Hopkins, E. Bond, J. A. Caggiano, D. A. Callahan, P. M. Celliers, C. Cerjan, D. S. Clark, S. N. Dixit, M. J. Edwards, N. Gharibyan, S. W. Haan, B. A. Hammel, A. V. Hamza, R. Hatarik, O. A. Hurricane, K. S. Jancaitis, O. S. Jones, G. D. Kerbel, J. J. Kroll, K. N. Lafortune, O. L. Landen, T. Ma, M. M. Marinak, B. J. MacGowan, A. G. MacPhee, A. Pak, M. Patel, P. K. Patel, L. J. Perkins, D. B. Sayre, S. M. Sepke, B. K. Spears, R. Tommasini, C. R. Weber, C. C. Widmayer, C. Yeamans, E. Giraldez, D. Hoover, A. Nikroo, M. Hohenberger, and M. Gatu Johnson, Physics of Plasmas **23**, 056303 (2016).
[27] V. A. Smalyuk, H. F. Robey, T. Döppner, D. T. Casey, D. S. Clark, O. S. Jones, J. L. Milovich, J. L. Peterson, B. Bachmann, K. L. Baker, L. R. Benedetti, L. F. Berzak Hopkins, R. Bionta, E. Bond, D. K. Bradley, D. A. Callahan, P. M. Celliers, C. Cerjan, K.-C. Chen, C. Goyon, G. Grim, S. N. Dixit, M. J. Eckart, M. J. Edwards, M. Farrell, D. N. Fittinghoff, J. A. Frenje, M. Gatu-Johnson, N. Gharibyan, S. W. Haan, A. V. Hamza, E. Hartouni, R. Hatarik, M. Havre, M. Hohenberger, D. Hoover, O. A. Hurricane, N. Izumi, K. S. Jancaitis, S. F. Khan, J. P. Knauer, J. J. Kroll, G. Kyrala, K. N. Lafortune, O. L. Landen, T. Ma, B. J. MacGowan, A. G. MacPhee, M. Mauldin, F. E. Merrill, A. S. Moore, S. Nagel, A. Nikroo, A. Pak, P. K. Patel, J. E. Ralph, D. B. Sayre, D. Shaughnessy, B. K. Spears, R. Tommasini, D. P. Turnbull, A. L. Velikovich, P. L. Volegov, C. R. Weber, C. C. Widmayer, and C. Yeamans, Physics of Plasmas **23**, 102703 (2016).
[28] A. L. Velikovich, F. L. Cochran, and J. Davis, Phys. Rev. Lett. **77**, 853 (1996).
[29] S. F. Khan, S. A. MacLaren, J. D. Salmonson, T. Ma, G. A. Kyrala, J. E. Pino, J. R. Rygg, J. E. Field, R. Tommasini, J. E. Ralph, D. P. Turnbull, A. J. Mackinnon, K. L. Baker, L. R. Benedetti, D. K. Bradley, P. M. Celliers, E. L. Dewald, T. R. Dittrich, L. Berzak Hopkins, N. Izumi, M. L. Kervin, J. L. Kline, S. R. Nagel, A. Pak, and R. E. Tipton, Physics of Plasmas **23**, 042708 (2016).
[30] F. H. Busse, Chaos **4**, 123 (1994).
[31] A. Hasegawa, C. G. Maclennan, and Y. Kodama, Physics of Fluids **22**, 2122 (1979).

[32]B. K. Spears, S. Glenzer, M. J. Edwards, S. Brandon, D. Clark, R. Town, C. Cerjan, R. Dylla-Spears, E. Mapoles, D. Munro, J. Salmonson, S. Sepke, S. Weber, S. Hatchett, S. Haan, P. Springer, E. Moses, J. Kline, G. Kyrala, and D. Wilson, Physics of Plasmas **19**, 056316 (2012).
[33]R. Nora, J. L. Peterson, B. K. Spears, J. E. Field, and S. Brandon, Statistical Analysis and Data Mining (2016 accepted).
[34]S. H. Langer, B. K. Spears, J. L. Peterson, J. E. Field, R. Nora, and S. Brandon, in *Proceedings of ISAV 2016: Second Workshop on In Situ Infrastructures for Enabling Extreme-scale Analysis and Visualization* (IEEE Computer Society, 2016).
[35]K. Rarick, http://kr.github.io/beanstalkd/.
[36]M. M. Marinak, G. D. Kerbel, N. A. Gentile, O. Jones, D. Munro, S. Pollaine, T. R. Dittrich, and S. W. Haan, Physics of Plasmas **8**, 2275 (2001).
[37]D. D.-M. Ho, S. W. Haan, J. D. Salmonson, D. S. Clark, J. D. Lindl, J. L. Milovich, C. A. Thomas, L. F. B. Hopkins, and N. B. Meezan, Journal of Physics: Conference Series **717**, 012023 (2016).
[38]G. H. Miller, E. I. Moses, and C. R. Wuest, Nuclear Fusion **44** (2004).
[39]G. I. Kerley, *Equations of State for Hydrogen and Deuterium*, Tech. Rep. SAND 2003-3613 (Sandia National Laboratories, 2004).
[40]P. A. Sterne, L. X. Benedict, S. Hamel, A. A. Correa, J. L. Milovich, M. M. Marinak, P. M. Celliers, and D. E. Fratanduono, Journal of Physics: Conference Series **717**, 012082 (2016).
[41]F. Pedregoas, G. Varoquaux, A. Gramfort, V. Michel, B. Thirion, O. Grisel, M. Blondel, P. Prettenhofer, R. Weiss, V. Dubourg, J. Vanderplas, A. Passos, D. Cournapeau, M. Brucher, M. Perrot, and E. Duchesnay, Journal of Machine Learning Research **12**, 2825 (2011).
[42]B. K. Spears, S. Brandon, D. Clark, C. Cerjan, J. Edwards, O. Landen, J. Lindl, S. Haan, S. Hatchett, J. Salmonson, P. Springer, S. V. Weber, and D. Wilson, Journal of Physics: Conference Series **244**, 022014 (2010).
[43]J. A. Nelder and R. Mead, The Computer Journal **7**, 308 (1965).
[44]C. R. Weber and B. A. Hammel, private communication (2016).
[45]O. A. Hurricane and J. Hammer, *Pressure Driven Instability of a Finite Thickness Fluid Layer*, Tech. Rep. UCRL-JRNL-203840 (Lawrence Livermore National Laboratory, 2004).
[46]R. Kishony and D. Shvarts, Physics of Plasmas **8**, 4925 (2001).
[47]K. Anderson, private communication (2016).
[48]D. S. Clark, private communication (2016).
[49]M. J. M. Hill, Proceedings of the Royal Society of London **55**, 219 (1894).
[50]J. Burgers, in *Advances in Applied Mechanics*, Vol. 1, edited by R. V. Mises and T. V. Kármán (Elsevier, 1948) pp. 171 – 199.
[51]T. Maxworthy, Journal of Fluid Mechanics **51**, 15 (1972).
[52]A. Prochazka and D. I. Pullin, Physics of Fluids **7**, 1788 (1995).
[53]C. R. Weber, D. S. Clark, A. W. Cook, L. E. Busby, and H. F. Robey, Phys. Rev. E **89**, 053106 (2014).
[54]D. Sharp, Physica D: Nonlinear Phenomena **12**, 3 (1984).
[55]R. Betti, private communication (2016).
[56]L. F. Berzak Hopkins, S. Le Pape, L. Divol, N. B. Meezan, A. J. Mackinnon, D. D. Ho, O. S. Jones, S. Khan, J. L. Milovich, J. S. Ross, P. Amendt, D. Casey, P. M. Celliers, A. Pak, J. L. Peterson, J. Ralph, and J. R. Rygg, Physics of Plasmas **22**, 056318 (2015).
[57]L. F. Berzak Hopkins, private communication (2016).
[58]S. Skupsky, J. A. Marozas, R. S. Craxton, R. Betti, T. J. B. Collins, J. A. Delettrez, V. N. Goncharov, P. W. McKenty, P. B. Radha, T. R. Boehly, J. P. Knauer, F. J. Marshall, D. R. Harding, J. D. Kilkenny, D. D. Meyerhofer, T. C. Sangster, and R. L. McCrory, Physics of Plasmas **11**, 2763 (2004).